I&EC research
Industrial & Engineering Chemistry Research

pubs.acs.org/IECR
Article

Atomistic Investigation of Viscoelastic Nanofluids as Heat Transfer Liquids for Immersive-Cooling Applications

Bharath Ravikumar, Ioannis K. Karathanassis,* Timothy Smith, and Manolis Gavaises

Cite This: https://doi.org/10.1021/acs.iecr.4c01832

ABSTRACT: A comparative assessment of the thermal properties and heat transfer coefficients achieved by viscoelastic nanofluids suitable for immersion cooling is presented, with the candidate samples exhibiting distinct differences based on the nanoparticle chemistry and shape. Molecular dynamics simulations of different nanoparticles such as copper nanosphere, two-dimensional pristine graphene, and single-walled carbon nanotube (CNT) dispersed in PAO-2 of concentrations of approximately equal to 2.6% by weight are performed in the present investigation. While carbon-based nanoparticles increase the specific heat capacity of the nanofluids, copper-based nanofluids show a decrease in the corresponding values. Moreover, the heat conduction in copper-based nanofluids is dependent on the higher degree of phonon density of states (DOS) matching between the copper and solvent atoms, whereas the high intrinsic thermal conductivity of graphene and CNT compensates for the lower degree of DOS matching. The addition of an OCP polymer chain to impart viscoelasticity in the nanofluids exhibits a heat transfer coefficient enhancement of more than 80% during Couette flow as a result of chain expansion, indicating their suitability for immersive-cooling applications.

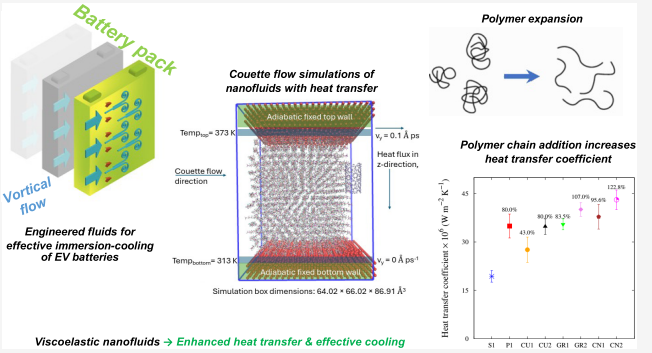

INTRODUCTION

The forthcoming regulations in Europe and the US for the phase-out of hydrofluorocarbon coolants (HFCs) used in a wide range of cooling systems and the necessity for replacement with environmentally friendly fluids with low global warming potential (GWP) render the implementation of numerical methodologies for the design of novel coolants timely.[1,2] In addition, there are stringent mandates in place for decarbonization of passenger cars and, eventually, heavy-duty vehicles, earth-moving machines, and aircraft, which, among other significant limitations (such as efficient energy storage, battery weight, safety, limited availability of carbon-free fuels, and cost), have to overcome the excess heat generated in electrified powertrains during power-demanding operations with which conventional cooling solutions employing air or water cannot cope.[3,4] One of the primary areas of interest for engineered cooling fluids is electric vehicle battery thermal management systems (EV BTMS). The existing methodologies of indirect cooling techniques in the BTMS involve a combination of air-cooling and liquid-cooling heat-sink devices and phase-change materials.[5] Such systems consist of several energy-consuming components such as pumps, motors, compressors, and chillers to maintain the operating temperatures favorable for the safety and long life of lithium-ion battery modules.[6] Therefore, an advanced mechanism to improve the efficiency of cooling by reducing parasitic power consumption and thermal contact resistances is essential for a sustainable EV rollout. One such mechanism being proposed is the immersive-cooling technique that can reduce the footprint of the BTMS in passenger vehicles[7] and increase the heat transfer coefficients achieved by 5 orders of magnitude compared to indirect air cooling.[8]

Given that immersive cooling involves battery modules directly submerged in liquid coolants, the options with respect to the involved working media are limited to dielectric fluids such as different types of silicone and mineral oils. However, ensuring minimal frictional losses and higher efficiency of thermal transport are essential characteristics required for immersive cooling. Therefore, additives are required to assist oil-based solvents in achieving these targets. The typical additives that are researched for enhancing the rheological properties of oils are polymer chains and surfactants. Experimental studies report the stabilization of vortices and reduction of thermal boundary layers due to the viscoelastic nature of the polymer chains.[9−11] Concurrently, a recent focus

Received: May 13, 2024
Revised: October 24, 2024
Accepted: November 6, 2024

on the use of nanoparticles to enhance the thermal properties[12] of common cooling liquids motivates the present investigation.

Post the definition of nanofluids by Choi and Eastman,[13] the vast majority of works on thermofluids deal with aqueous nanofluids consisting of metal, metal oxide, or carbon allotrope nanoparticles.[14−18] The dependence of size, concentration, and defects of the nanoparticles on the thermal properties of the aqueous nanofluids is discussed in the literature.[19−22] The exposure toward oil-based nanofluids is focused on enhancing the thermal and rheological properties of lubricants and engine oil,[23−25] and the latest experimental research studies pursue their identification. Cai et al.[26] reported how the Nusselt number increases by 40% when pristine graphene is dissolved in heavy-duty diesel engine oil. The measurements of Aberoumand and Jafarimoghaddam[27] showed that a 1% weight fraction of copper nanoparticles in engine oil enhances the thermal conductivity by 49%. However, the mechanism of heat transfer is specific to the chemical structure of the fluids, as suggested by the studies of Jin et al.[28] and Alosious et al.[29] Hong et al.,[30] showed experimentally that higher thermal conductivity of the elements of nanoparticles does not always improve thermal properties of the nanofluids. The empirical models to compute effective thermal conductivity of solid−liquid suspensions such as the Maxwell model,[31] Hamilton−Crosser model,[32] Davis model,[33] Lu-Lin model,[34] Yu and Choi model,[35] and Jang and Choi model[36] based on conventional continuum theories are limited to specific systems. Such limitations of numerical simulations based on continuum mechanics are being dealt with using deep learning techniques such as artificial neural networks (ANNs) to an extent.[37,38] However, such data-intensive techniques still require physical insights at the atomistic scale to optimize heat transfer fluid mixtures. Thus, a detailed atomistic exploration is necessary to prescribe the optimal additives necessary to enhance the heat transfer capabilities of different nanofluids. In this research, the emphasis is on dilute viscoelastic nanofluids that are formed by the addition of polymers and nanoparticles in a base solvent. A thorough study to understand the impact of the combination of polymer and nanoparticle additives in an oil solvent and the underlying mechanism of heat transfer of such fluids is still lacking in the open literature.

Molecular dynamics (MD) simulation is utilized here to compute the thermophysical properties of the nanofluids and provide insights into the mechanism of heat transfer. As the nanofluids are dependent on the chemistry of the nanoparticles and their behavior in the liquid mixture, the study here considers three different types of nanoparticles, namely, copper (Cu) nanosphere representing metallic nanoparticles, two-dimensional (2D) pristine graphene, and single-walled carbon nanotube (CNT). These different classes of nanoparticles are shown to be industrially relevant for lubrication as well as heat transfer applications.[39,40] The base oil solvent is chosen as polyalphaolefin (PAO-2) with a kinematic viscosity of approximately 2 cSt at 373 K, and to impart viscoelastic nature to the nanofluids, an olefin copolymer (OCP) is dispersed in the different fluids. The elasticity imparted with the addition of polymer chains has recently been demonstrated to decrease the thermal boundary layer and improve the Nusselt numbers in laminar flows.[41] Additionally, the polymer chains can stabilize the secondary-flow motion, in turn leading to boundary layer disruption.[11] PAO-2 emerges as an essential solvent for several lubricants due to its high fluidity at lower temperatures and high chemical stability necessary for heat transfer applications.[42] On the other hand, the linear architecture and narrow molecular weight distribution make OCP a useful additive for industrial applications.[43,44]

Nanofluids of concentrations of approximately 2.6% by weight are simulated in the temperature range of 313 and 373 K. The choice of concentration is made after probing the literature on industrially relevant nanofluids, which recommends the use of nanofluids below 3 wt % to ensure smooth circulation and prevention of corrosion.[45] The force field model selection of the different molecules is done after a preliminary investigation of the different structural and transport properties. The reported force field parameters using hybrid potentials would be of interest to the research approaches on nanofluid modeling. Post a thermodynamic stability analysis, heat transfer properties such as specific heat capacity and thermal conductivity are reported for the different nanofluids, following which the mechanism of heat transfer is analyzed. The casings of batteries in the packs used in EVs are made of steel, aluminum, or plastic.[46] The heat transfer fluids are essentially in contact with these casings during immersion cooling. Therefore, the heat transfer coefficient of the nanofluids flowing through a nanochannel formed by solid iron (Fe) layers and the role of viscoelasticity in the enhancement of the thermal dissipation of nanofluids are discussed. The structural mechanism of heat transfer in oil-based nanofluids discussed aims to assist in the adoption of such nanofluids for immersive-cooling applications. To the authors' knowledge, the present work constitutes the first investigation in the open literature leveraging MD simulations to estimate the thermal properties of complex-rheology fluids in a Couette flow where nanoparticles are also dispersed, providing an updated understanding of the optimal design of such systems.

MODELING AND SIMULATION

Simulation Methodology. Equilibrium MD simulations are initially performed on bulk fluids to verify the modeling approach and compute the pertinent thermophysical properties. The pure PAO-2 solvent (S1) simulation box is created using 340 molecules of 9,10-dimethyloctadecane.[47] The OCP polymer chain studied here is made up of 50 mol % ethylene (C2) monomers and 50 mol % propylene (C3) monomers with a molecular mass of 3016 g mol^{-1} (Fluid P1), in agreement with the approach followed in the previous study of the authors.[48] The schematics of PAO-2 and OCP are provided in Figure S1 in the Supporting Information. The chain consists of 43 molecules, each of C2 and C3 monomers, with the two ends of the chain terminated using hydrogen atoms. A copper nanosphere of a diameter of 1 nm is dispersed in the solvent as well as the polymer solution to create Cu nanofluids (Fluids CU1 and CU2). Graphene nanofluids (GR1 and GR2) contain four 2D graphene molecules of long diagonal length 1.2 nm. Similarly, CNT nanofluids (CN1 and CN2) are generated by adding a CNT of the length of 1.5 nm, diameter of 0.985 nm, and chiral index of (4,10). The selection of this specific number of molecules corresponds to nanoparticle concentrations of ≈2.6 wt %, typical of oil-based nanofluids of industrial requirements.[49] For copper nanofluids, two higher concentrations with 2 and 4 nanoparticles representing 5.5 and 11 wt %, respectively, are also simulated to study the stability aspects. The polymer fluids represent a weakly viscoelastic liquid, given the chain size and weight of the polymer used. At room temperature, the intrinsic thermal

https://doi.org/10.1021/acs.iecr.4c01832
Ind. Eng. Chem. Res. XXXX, XXX, XXX−XXX

conductivity of copper nanoparticles is reported to be of the order of 400 W m^{-1} K^{-1}, while that of 2D graphene and CNT range up to 5000 and 6600 W m^{-1} K^{-1}, respectively.[50,51] Table 1 shows the concentration of the additives in the different simulated nanofluids.

Table 1. Concentration (by Weight %) of Additives in the Different Nanofluids

fluid	name	additive concentration	
		polymer	nanoparticle
PAO-2	S1		
PAO-2 + 1 OCP	P1	3.04	
PAO-2 + 1 Cu	CU1		2.77
PAO-2 + 1 Cu + 1 OCP	CU2	2.97	2.69
PAO-2 + 4 graphene	GR1		2.63
PAO-2 + 4 graphene +1 OCP	GR2	2.97	2.55
PAO-2 + 1 CNT	CN1		2.54
PAO-2 + 1 CNT + 1 OCP	CN2	2.97	2.46

Periodic boundary conditions (PBC) are applied in all 3 directions. A Nosé−Hoover thermostat is implemented to maintain the temperatures at equilibration and production runs of the equilibrium MD between 313 and 373 K. The corresponding Parrinello−Rahman barostat, as implemented by LAMMPS (NPT), is used to set the pressure at 1 atm during the equilibration phase. The distance cutoff for van der Waals interactions is set to 13 Å. A faster Ewald summation methodology called particle−particle−particle mesh (PPPM) is used to compute the long-range electrostatic interactions. The velocity Verlet algorithm is used to integrate the equations of motion with a time step of 1 fs.

1−4 intramolecular non-bonded pairwise interactions are given a weight of 0.5 for solvent-based fluid simulations, whereas it is switched off in case of the simulations of polymer-based fluid simulations. Energy minimization and equilibration under NPT is carried out for 20 ns, after which a production run of 40 ns under NVT ensemble is performed. The system, after the 40 ns run, is utilized for rNEMD simulations to compute the thermal conductivity. In rNEMD simulations, a linear temperature gradient along the z-direction is implemented, as described by Müller-Plathe.[52] The subsequent heat flux is utilized to measure the thermal conductivity values. The reported results of the different properties are averages of three independent simulations, with the corresponding standard deviations shown in the appropriate figures.

For simulating the heat transfer during Couette flow between a channel of Fe plates, a simulation box is used that has PBC in x- and y-directions (see Figure 1). The boundary in the z-direction is fixed (non-periodic), and the heat transfer liquids are placed between the layers of Fe atoms. The PPPM method is modified here by using the slab option in LAMMPS with a volume factor of 3.0 to obtain accurate electrostatics in the absence of periodicity in the z-direction.[53] The outermost 6 layers of Fe on both ends of the z-direction have the interactions switched off, and a wall repulsion force is used to represent an adiabatic system. The boundary conditions enable the fluid atoms to be confined between the internal faces of the solid Fe atoms. The systems are energy minimized to avoid any unphysical configurations. The systems are equilibrated at 313 K using NVT for 4 ns before the innermost two layers of Fe are maintained at 373 K (top layer) and 313 K (bottom layer), respectively, using a Langevin thermostat.[54] The top layer at

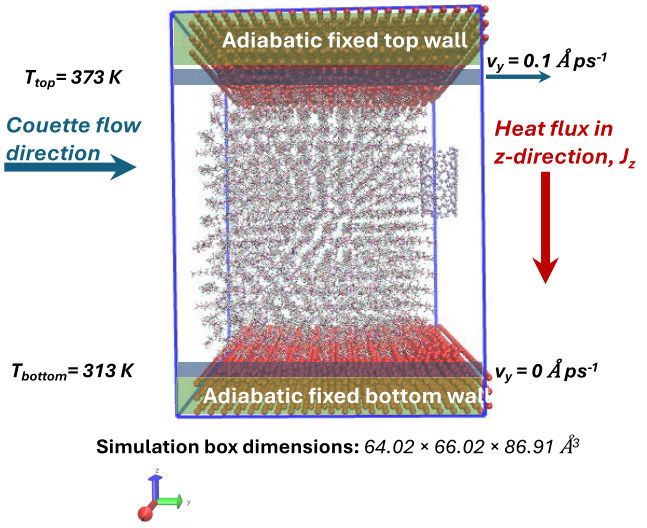

Figure 1. Simulation box of nanofluid CN1 after the energy minimization step. Atoms in red at the top and bottom represent Fe.

373 K is moved in the y-direction at $v_{y,max}$ = 0.1 Å ps^{-1}, and the bottom Fe layer at 313 K is kept stationary by switching off the velocities in both y- and z-directions. The simulation setup generates a Couette flow nanochannel with a heat flux from the top Fe layer to the bottom Fe layer via the liquids.

Model Selection. A vast array of models and corresponding parameters are available in the literature for the nanoparticles being considered in this research.[28,55−66] Therefore, a fundamental investigation of the suitability of these models and parameters needs to be performed for the simulated heterogeneous nanofluids. The selection process is accomplished by analyzing the stability of the nanoparticles visually in the nanofluids, structural radial distribution function, as well as trends of density and viscosity as a function of temperature.

Multibody embedded atom model (EAM) potential of the following functional form

$$V_{\mathrm{EAM}} = \sum_i E_i(\rho_{\mathrm{h},i}) + \frac{1}{2}\sum_i \sum_{j\neq i} \Phi_{ij}(R_{ij}) \tag{1}$$

is used to model the interactions between Cu atoms of the nanoparticles, as they are reported to exhibit atomic cohesion and accurate phonon spectra essential to compute structural and thermal properties for our study. Here, $E_i(\rho_{\mathrm{h},i})$ is the energy to embed atom i into the background host electron density, $\rho_{\mathrm{h},i}$ and $\Phi_{ij}(R_{ij})$ are the core−core pair repulsion between atoms i and j separated by the distance R_{ij}. Foiles et al.[57] have provided a tabulated set of EAM potential parameters for Cu atoms, which are used in the present study.

To describe the graphene and CNT intramolecular nanoparticle interactions, a bond-order potential formulated by Tersoff of the following basic analytical form

$$V_{\mathrm{Tersoff}} = \sum_{i>j} f_c(r_{ij})(V_{\mathrm{R}}(r_{ij}) - b_{ij}V_{\mathrm{A}}(r_{ij})) \tag{2}$$

is predominantly utilized.[67] Here, $V_{\mathrm{R}}(r_{ij})$ and $V_{\mathrm{A}}(r_{ij})$ represent the competing repulsive and attractive bond potentials, with $f_c(r_{ij})$ acting as the cutoff term, ensuring that only nearest-neighbor interactions are accounted for. The bond order between atoms i and j in eq 2 is given by b_{ij}. Among the different first-principles-based parametrizations available in the

https://doi.org/10.1021/acs.iecr.4c01832
Ind. Eng. Chem. Res. XXXX, XXX, XXX−XXX

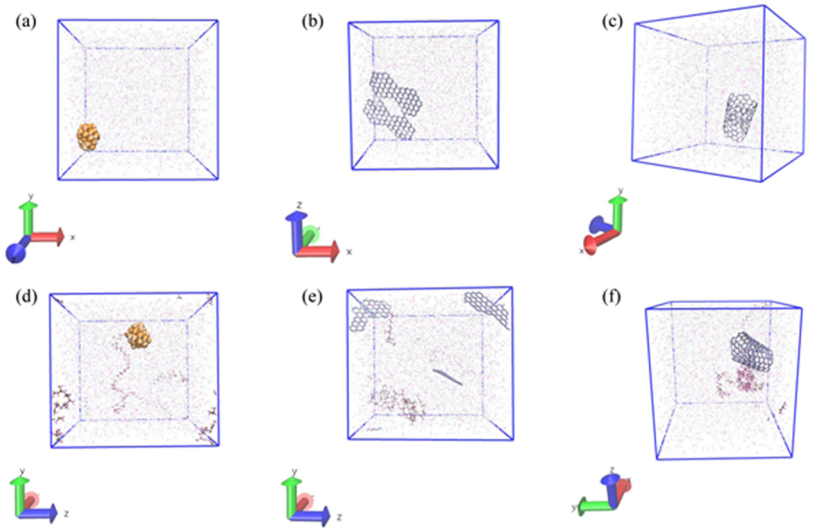

Figure 2. Simulation box of nanofluids (a) CU1, (b) GR1, (c) CN1, (d) CU2, (e) GR2, and (f) CN2 at the end of the NPT equilibration run at 313 K. The orange-colored atoms represent Cu in panels (a, d). The purple-colored atoms represent 2D graphene in panels (b, e) and CNT in panels (c, f). The pink atoms represent the OCP polymer chain in panels (d–f). The translucent atoms represent the PAO-2 solvent in all the simulation boxes.

literature for Tersoff potentials of carbon, the optimized parameters prescribed by Erhart and Albe[60] possess good transferability while handling hybrid potentials as the ones in this study.

At the same time, it is essential to select the optimal LJ parameters that work well with the selected solid-state potentials in the simulated chemical mixtures. Therefore, the LJ parameters for van der Waals interactions between the nanoparticles and the solvent/polymer are selected after a preliminary investigation of parameters available in the literature.[28,55,58,63,64,66] The parameters of PAO-2 and OCP are obtained from the L-OPLS-AA force field.[68,69] The LJ parameters and the partial charges of the different atoms are tabulated and shown in Tables S1 and S2, respectively, in the Supporting Information.

The different nanofluid mixtures are listed in Figure 2. The selected final parameters show Cu nanoparticles remain intact and atoms do not disintegrate (see Figure 2a,d). Further discussion of the thermodynamic stability of the nanofluids is conducted in the Results and Discussion section. The 2D graphene molecules showcase aggregation at the concentrations simulated (see Figure 2b,e), which is in line with its experimental findings.[70,71] The CNT nanoparticle retains a cylindrical shape with limited shape changes (see Figure 2c,f). The density of the copper, graphene, and CNT nanofluids showcase higher values compared to the solvent at all the temperatures, exhibiting a linear decrease as a function of temperature (refer to Figure 3). Among the nanofluids simulated, CU2 shows the highest density at different temperatures (e.g., 0.805 g cm^{-3} at 313 K), reflecting the mass and concentration of the copper and OCP additives in the nanofluids.

The pairwise radial distribution function (RDF), $g_{o,p}(r)$, is computed using the equation

$$g_{o,p}(r) = \frac{n(r)}{4\pi\rho_{n,p}r^2\delta r} \quad (3)$$

where $n(r)$ is the number of p atoms, with a number density $\rho_{n,p}$ in the simulation box, present in a spherical shell of

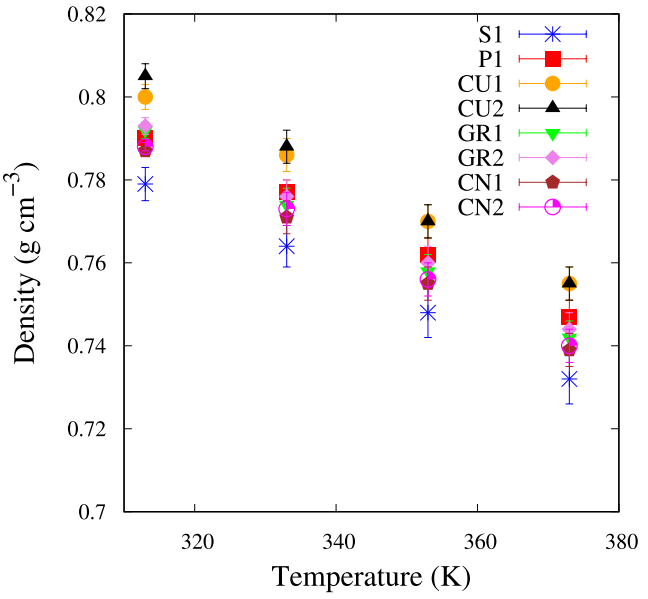

Figure 3. Density of the simulated fluids as a function of the temperature. The error bars correspond to standard deviations from three independent runs.

thickness δr from the central atom o. Figure 4 shows the RDF values of the carbon atoms of the solvent and nanoparticles. $g_{C_{solvent},Cu}(r)$ shows an initial peak at 3.35 Å, and $g_{H_{solvent},Cu}(r)$ shows the peak at 2.35 Å. This is comparable with the study by Zhang et al.,[72] where the distance between Cu and C shows the initial peak at 3.35 Å. Similarly, $g_{C_{solvent},C_{graphene}}(r)$ and $g_{C_{solvent},C_{CNT}}(r)$ indicate two short peaks between 3 and 4 Å, and between 4 and 4.5 Å. Kuziel et al.[73] show similar RDF peaks at these distances between the hydrophobic 2D graphene surface and the carbon atom of oil. Thus, it provides us evidence of the models' ability to demonstrate appropriate dissolution of the nanoparticles in the nanofluids.

The Green–Kubo method based on the fluctuation–dissipation theorem of systems in equilibrium is used to find

https://doi.org/10.1021/acs.iecr.4c01832
Ind. Eng. Chem. Res. XXXX, XXX, XXX–XXX

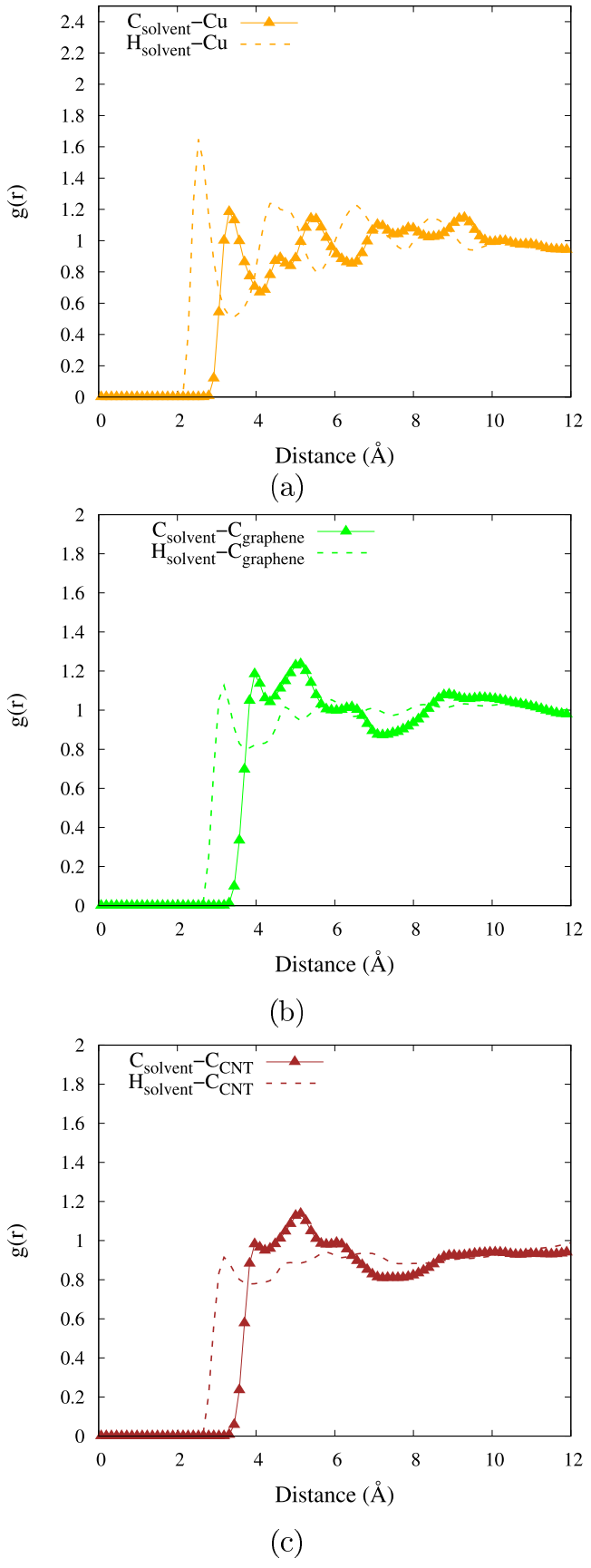

Figure 4. Radial distribution functions: (a) $g_{C_{solvent}Cu}(r)$ in CU1, (b) $g_{C_{solvent}C_{graphene}}(r)$ in GR1, and (c) $g_{C_{solvent}C_{CNT}}(r)$ in CN1 at 313 K.

the zero-shear dynamic viscosity (η_0).[74] It is computed by the integration of a decaying stress autocorrelation function, such that

$$\eta_0 = \frac{V}{k_B T}\int_0^\infty \langle \sigma_{xy}(t)\sigma_{xy}(0)\rangle \mathrm{d}t \tag{4}$$

Here, V is the volume of the simulation box, k_B is the Boltzmann constant, and $\sigma_{xy}(t)$ is one of the off-diagonal components of the stress tensor at time t. The statistics of η_0 computation are improved by taking an average of the autocorrelation function of the three off-diagonal components of the stress tensor. Figure 5 depicts the η_0 values of the

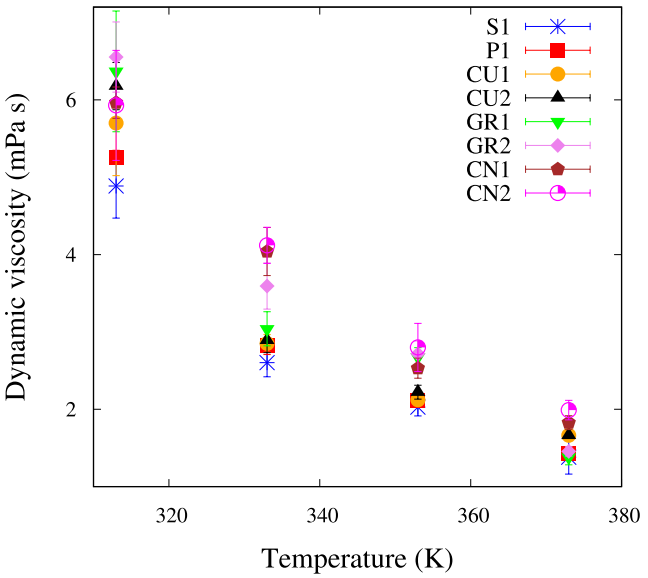

Figure 5. Zero-shear dynamic viscosity of the simulated fluids as a function of temperature. The error bars correspond to standard deviations from three independent runs.

different fluids simulated at various temperatures between 313 and 373 K. Nanoparticles increase the viscosity of the resultant nanofluids, with further addition of the OCP polymer raising the η_0 values at all the temperatures. Under shear forces, the simulated fluids showcase shear thinning beyond a shear rate of 10^9 s^{-1}, as demonstrated in Figure S2 in the Supporting Information. A Carreau model of the form

$$\eta(\dot{\gamma}) = \frac{\eta_0}{(1 + (\tau_s\dot{\gamma})^2)^m} \tag{5}$$

is fitted to the data, with τ_s representing the time constant referring to the shear rate where the shear thinning begins and m representing the strain-rate sensitivity coefficient. While comparing the fitting parameter τ_s of the model at 313 K in Table S3, we observe that the addition of the OCP polymer chain (as in the case of P1, CU2, GR2, and CN2) drives the resultant fluid mixtures to shear thin at lower shear rates (inverse of τ_s). While the η_0 values computed using eq 5 of fluids with suspended nanoparticles and polymers show higher values than the solvent dynamic viscosity, they vary (20−40%) from the η_0 computed using eq 4. This is observed in the literature and attributed to both the choice of force field and the selection of shear rate sampling at lower shear rates.[47,75]

The results presented here demonstrate that the models are suitable for investigations in the research. Thus, the systems

https://doi.org/10.1021/acs.iecr.4c01832
Ind. Eng. Chem. Res. XXXX, XXX, XXX−XXX

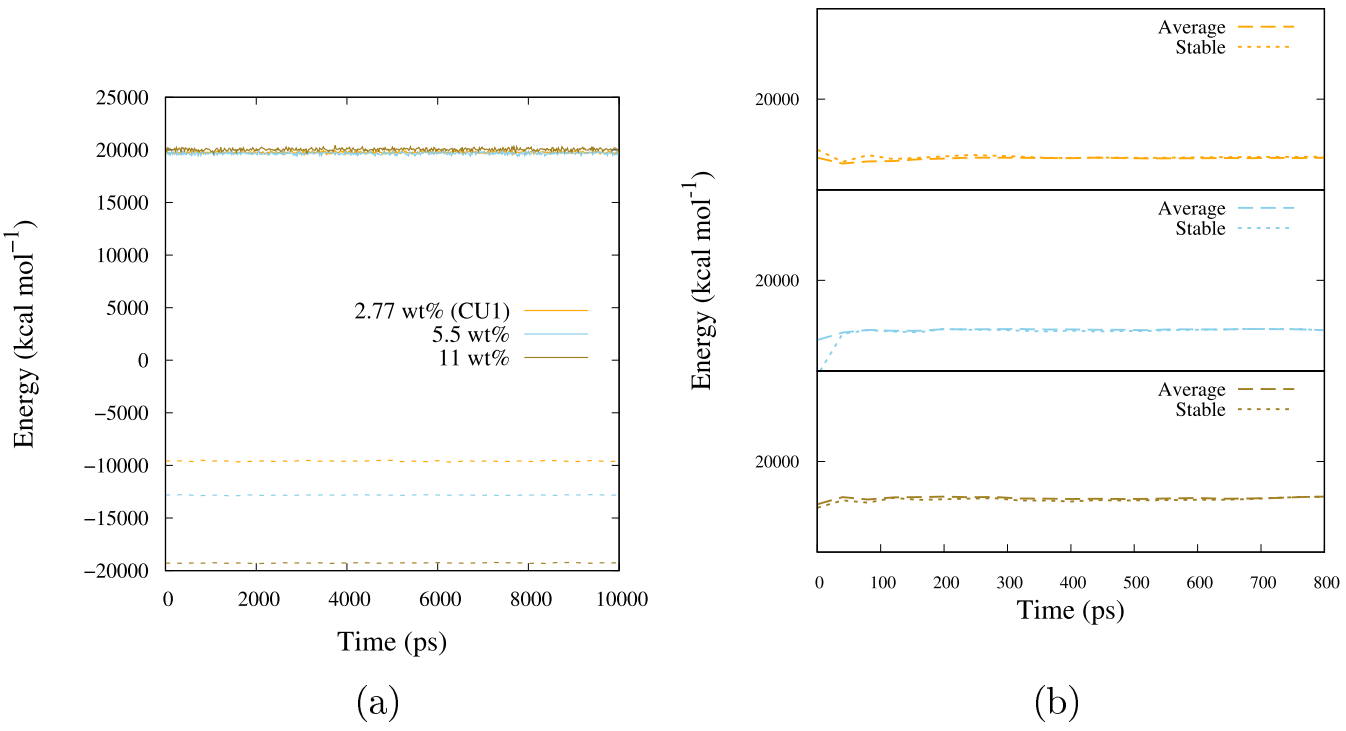

Figure 6. (a) Kinetic energy (solid lines) and non-bonded energy (dashed lines) of copper nanofluids at different concentrations as a function of time. (b) Running averages of kinetic energy of the stable configuration (dotted lines) and the mean of kinetic energy of all simulated configurations (dashed lines) as a function of time −2.77 wt % (top), 5.5 wt % (middle), and 11 wt % (bottom).

are further simulated to compute the thermal properties of the different fluids.

RESULTS AND DISCUSSION

Stability Analysis. The thermodynamic stability of the nanofluids is inspected to understand the binding of the nanoparticles with the surrounding media in the solutions. The interaction energies and kinetic energy statistics are utilized to understand the long-term and short-term stability of the nanofluids, as discussed in the literature.[20,21] Additionally, the solvation strength of the nanoparticles is analyzed using the potential of mean force (PMF) computed as

$$\mathrm{PMF} = -RT\ \ln(g(r)) \tag{6}$$

where R is the universal gas constant. The PMF value of solvation is computed from the depth of the first trough of the PMF data as a function of radial distance (r).

Figure 6a shows the different energies as a function of simulation time for various concentrations (2.77−11 wt %) of the copper-based nanofluids at 313 K. The non-bonded energy as well as kinetic energy converge to equilibrium values for all the concentrations, indicating a stable thermal equilibrium in the long run. Additional evaluation of the running average of kinetic energies of the Cu-based nanofluids, as demonstrated in Figure 6b, and comparison with the mean of different configurations show that the nanoparticle structures form a stable structure within 200 ps at all the concentrations. While probing the structures using visual molecular dynamics (VMD), we observe the nanoparticles, once aggregated within a few picoseconds, form a stable structure at all of the concentrations simulated. However, as the number of nanoparticles increases with the concentration, the size of the aggregate also increases (see Figure S3). This leads to a decrease in the surface coverage of the solvent molecules around the aggregated structures. This is reflected when comparing the PMF of the nanoparticle−solvent interactions, as shown in Figure 7. PMF magnitudes monotonically decrease from 0.328 kcal mol^{-1} at the concentration of CU1 to 0.112 kcal mol^{-1} at 11 wt %. While this is the case for solvation stability, the comparison of thermal conductivities does not exhibit a significant rise in the values (<0.1 W m^{-1} K^{-1}) as the

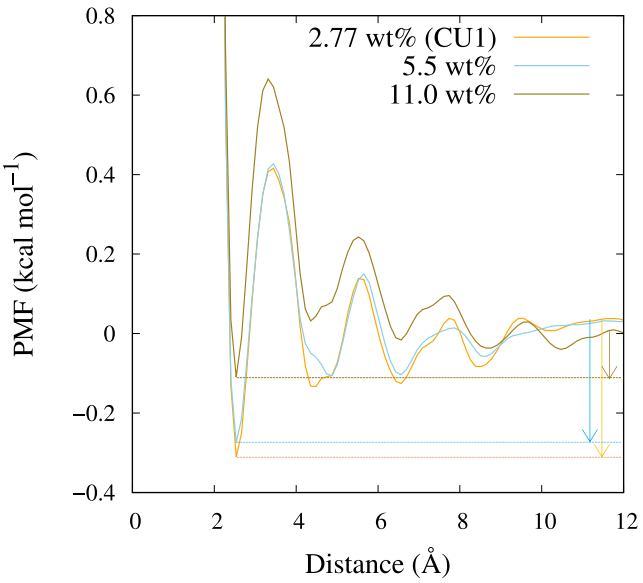

Figure 7. Potential of mean force (PMF) of nanoparticle−$H_{solvent}$ as a function of the radial distance at different concentrations. The arrows show the respective PMF of the solvation shells at 2.77 wt % (−0.328 kcal mol^{-1}), 5.5 wt % (−0.290 kcal mol^{-1}), and 11.0 wt % (−0.112 kcal mol^{-1}).

https://doi.org/10.1021/acs.iecr.4c01832
Ind. Eng. Chem. Res. XXXX, XXX, XXX−XXX

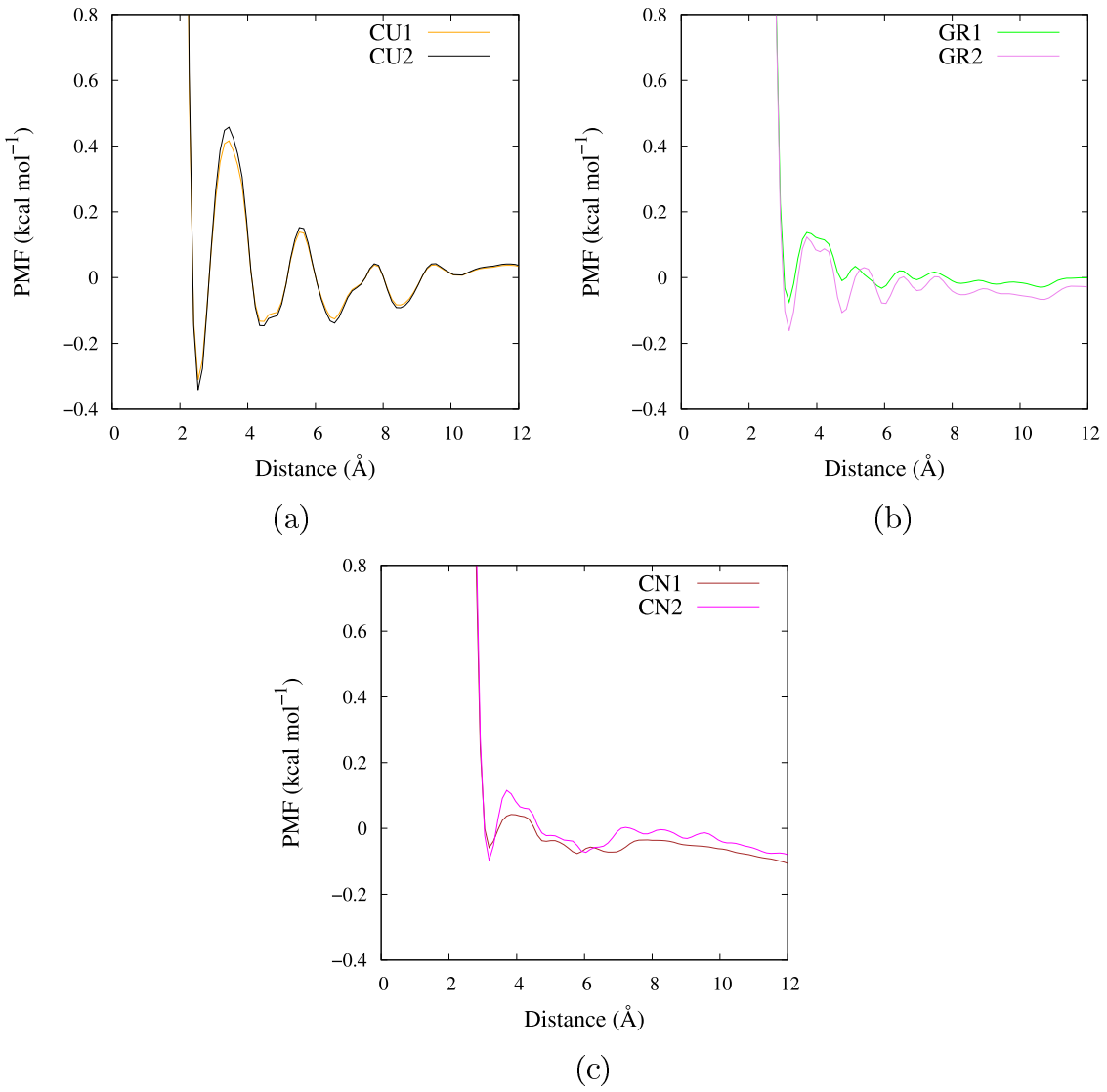

Figure 8. Potential of mean force (PMF) of nanoparticle−$H_{solvent}$ interactions as a function of radial distance for (a) CU1 and CU2, (b) GR1 and GR2, and (c) CN1 and CN2.

concentration increases (Figure S3). In the literature, an increase in concentration leads to a significant rise in thermal conductivity values while the increase in the size of the nanoparticles leads to a relevant decrease.[19] Thus, a competitive effect, also observed in the case of aqueous solutions in the literature,[22] where a volume fraction rise of 3.25% leads to a thermal conductivity increase of less than 0.2 W m^{-1} K^{-1} at 313 K, is seen here. In this work, the volume fraction difference between the lowest (2.77 wt %) and highest concentration (11 wt %) simulation is only 1.75%.

The comparison of the PMF values for the nanofluids of compositions shown in Table 1 is performed. Figure 8 indicates how the addition of the OCP polymer chain impacts the solvation stability of the different nanofluids. While CU1 shows a PMF magnitude of 0.328 kcal mol^{-1}, CU2 shows a slightly higher PMF magnitude of 0.360 kcal mol^{-1}. The trend is similar in the cases of GR1 (0.062 kcal mol^{-1}) and GR2 (0.179 kcal mol^{-1}). However, the addition of OCP does not seem to change the PMF value of CN2 significantly compared to that of CN1. The addition of the OCP chain thus seems to raise the interaction strength of the copper and graphene nanoparticles by the solvent molecules.

Thermal Properties. The specific heat capacity (C_p) of a liquid is computed in an MD simulation using the simplified equation

$$C_p = \frac{\langle E_{total}^2 \rangle - \langle E_{total} \rangle^2}{M_s R T^2} \quad (7)$$

where E_{total} is the total energy of the simulation box, M_s is the total mass of the simulation box, and R is the universal gas constant.[76,77]

Figure 9a shows the values of C_p as a function of the temperature for the different liquids. C_p of PAO-2 increases from 6194 J kg^{-1}K^{-1} at 313 K to 6400 J kg^{-1}K^{-1} at 373 K. The values are higher than the experimental C_p values by a minimum of 2.6 times, and the deviations are addressed as a limitation of OPLS-AA force fields due to the high energy of classical harmonic bond oscillator vibrations.[78] For the same temperature range, the experimental C_p values range from 2260 J kg^{-1}K^{-1} at 311 K to 2455 J kg^{-1}K^{-1} at 368 K.[79] However, the main objective of the study is to examine the influence of

https://doi.org/10.1021/acs.iecr.4c01832
Ind. Eng. Chem. Res. XXXX, XXX, XXX−XXX

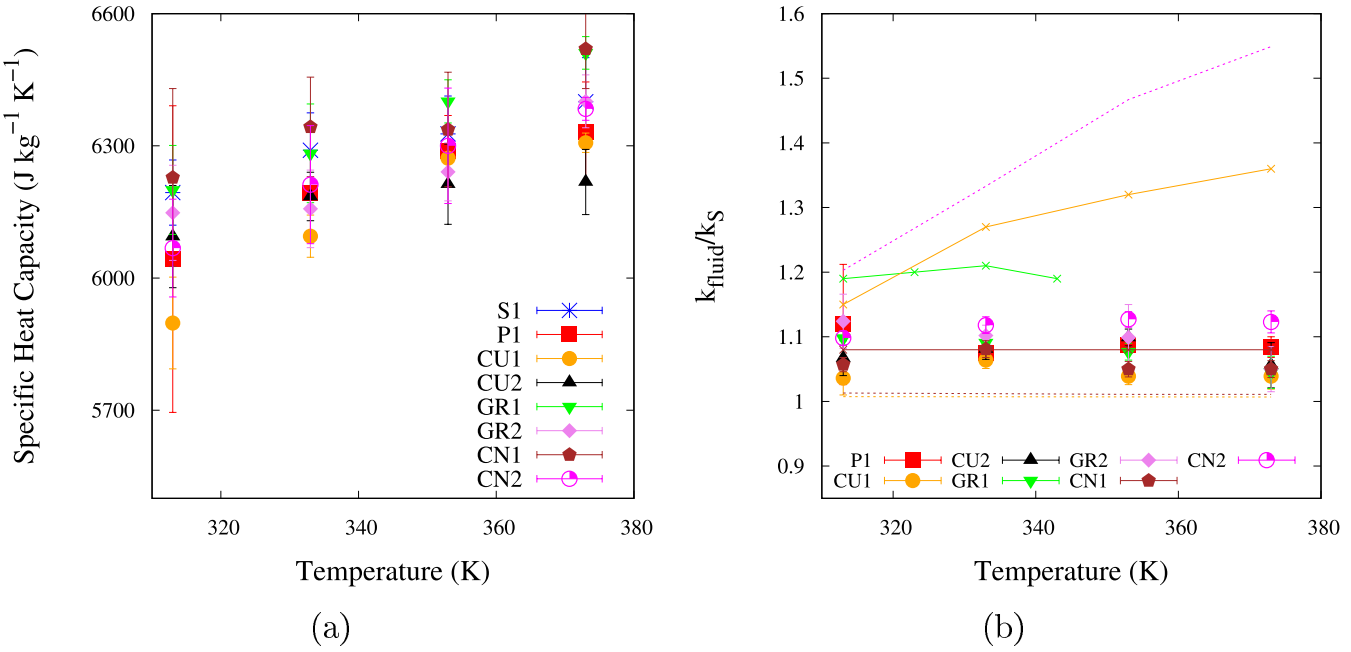

Figure 9. (a) Specific heat capacity (C_p) of the simulated fluids as a function of temperature. (b) $\frac{k_{fluid}}{k_S}$ of the simulated fluids with additives as a function of temperature. Simulated results are shown by markers with standard deviations. The dashed lines in panel (b) represent the values estimated by the different theoretical models for the nanofluids of respective volume fractions, such as by Maxwell[31] (orange), Hamilton−Crosser[32] (brown), and Fakoor Pakdaman et al.[82] (magenta). The solid lines in panel (b) represent the experimental results of 1 wt % oil-based copper nanofluid[27] (orange), 3 wt % oil-based graphene nanofluid[26] (green), and 1 wt % PAO-2-based MWCNT nanofluid[83] (brown).

polymers and nanoparticles on the thermal properties of the suspensions rather than on the absolute property values. Moreover, the prediction of thermal conductivity trends, as reported later with the different additives, is in line with the various experimental results and theoretical models.

As observed, the addition of the OCP polymer chain decreases the C_p values at all temperatures. A similar observation is made when Cu nanospheres are added to both the solvent and the OCP polymer solution. However, GR1 and CN1 nanofluids indicate higher C_p values than the base solvent. This is reflected in the independent experimental studies of Cai et al.[26] and Singh et al.[80] of 2D carbon-based nanoparticles dispersed in oils. On the other hand, the addition of OCP in 2D graphene and CNT polymer solutions leads to a competing effect of the C_p-enhancing nanoparticles and C_p-diminishing polymer chain. This leads to the C_p values of GR2 and CN2 nanofluids being lower than those of the solvent at all of the temperatures simulated. The specific heat capacity of solids such as the nanoparticles in the simulated systems is considered as the sum of the electronic and phonon contributions. For all practical purposes, i.e., temperatures above 10 K, the C_p of the nanoparticle is predominantly due to the phonon contribution.[81] The contrasting impact due to copper- and carbon-based nanoparticles on the C_p values of the simulated nanofluids may emerge from the differences in their respective phonon dispersion curves. Having understood the capabilities of the different nanofluids in thermal storage, it is important to estimate their thermal transport properties.

For a fluid oriented toward heat transfer applications, thermal conductivity (k) is a vital property to be computed. This metric provides a measure of the ability of a fluid to conduct heat, given a temperature gradient across it. It is also necessary for the computation of the Nusselt number of novel liquids characterizing the ratio of heat transfer via flow convection and conduction.[84] The conduction of heat is due to the microscopic behavior of the material, constituting MD as a useful tool to compute it.[85,86] The Müller-Plathe[52] methodology is used to compute thermal conductivity, and k of the heat transfer fluids is simulated. The formulation is based on the following relationship as given by Fourier's law

$$q = k\nabla T \tag{8}$$

where q is the heat flux across the fluid and ∇T is the corresponding temperature gradient. The Müller-Plathe methodology implements the ∇T by routinely exchanging the translational velocities of the atoms in the simulation box, conserving momentum. Over a long time period, the continuous exchange of momentum leads to the development of a linear ∇T across the simulation box. The computed k values of the different fluids and the corresponding available experimental data are compared in Table S4 in the Supporting Information.

To compare how the different additive-mixed fluids perform against the base solvent, the ratio $\frac{k_{fluid}}{k_S}$ is computed. Figure 9b depicts the $\frac{k_{fluid}}{k_S}$ values of the different heat transfer fluids as a function of temperature. OCP and the different nanoparticles lead to an increase in the thermal conductivity of the resultant fluids. The average thermal conductivity of fluid P1 shows an increase of 12% compared to solvent S1 at 313 K, whereas CU1 shows an increase of 4%. GR1 and CN1 exhibit increases of 10 and 6%, respectively, at 313 K. The addition of the OCP polymer chain increases the overall thermal conductivity of the nanofluids even though the appreciation is different for the different nanofluids. While CU2 shows a further enhancement of k by 3% compared to that of CU1, the ratios for GR2 and CN2 increase by an additional 1.6% compared to GR1 and

https://doi.org/10.1021/acs.iecr.4c01832
Ind. Eng. Chem. Res. XXXX, XXX, XXX−XXX

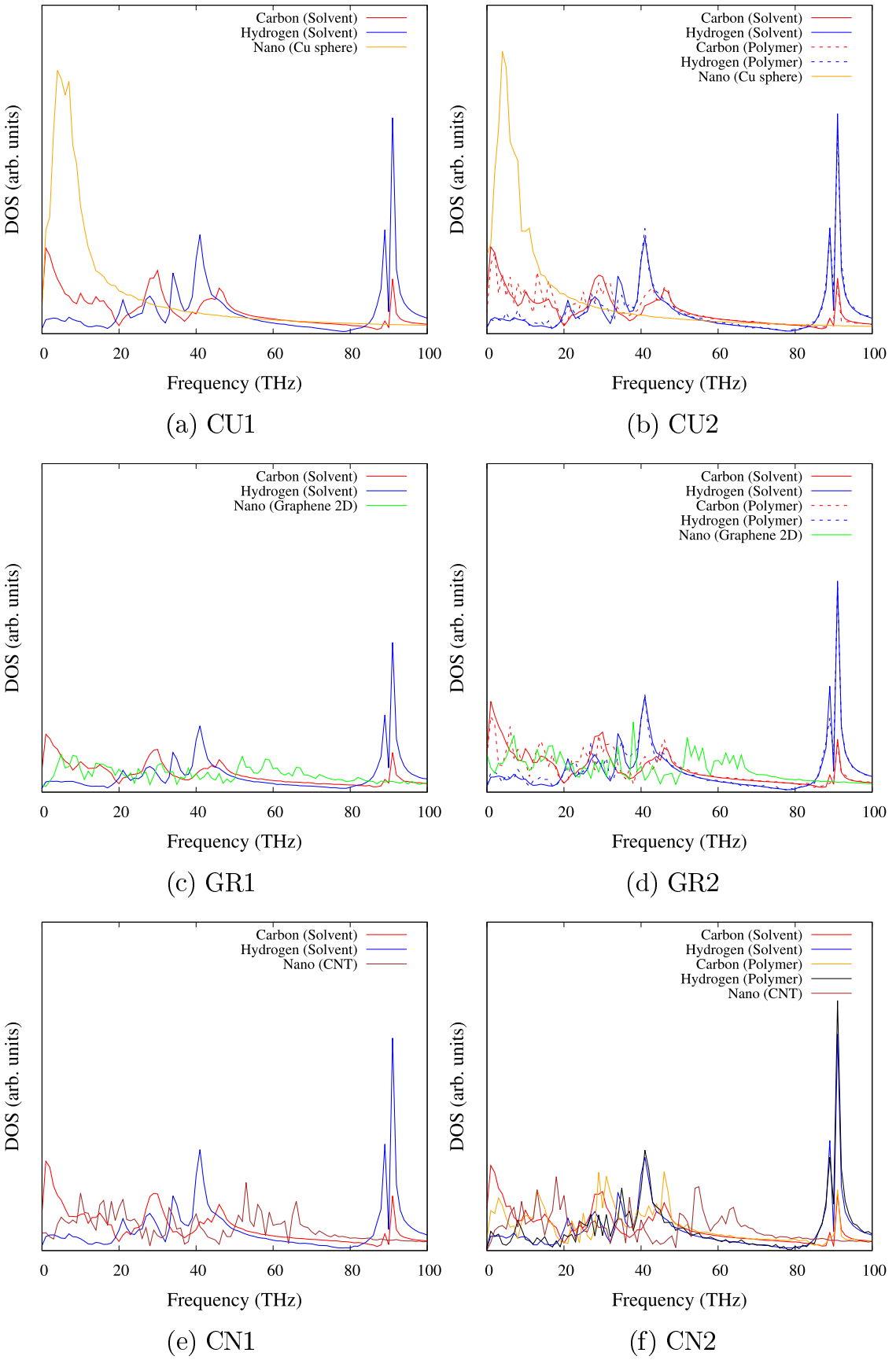

Figure 10. Phonon vibrational density of states (DOS) of the different nanofluids at 313 K.

https://doi.org/10.1021/acs.iecr.4c01832
Ind. Eng. Chem. Res. XXXX, XXX, XXX−XXX

CN1, respectively. Most importantly, the addition of OCP in CNT-based nanofluids increases $\frac{k_{fluid}}{k_S}$ as temperature increases from 313 to 373 K.

Figure 9b compares the results of the different simulated nanofluids to theoretical models and the available oil-based nanofluid experimental results. As observed, the traditional solid suspension models by Maxwell[31] and Hamilton−Crosser[32] using the same volume fractions (0.0019−0.0025) as that of the simulated fluids predict lower $\frac{k_{fluid}}{k_S}$ ratios. While the Maxwell model is suitable for spherical particles, the Hamilton−Crosser model is used to find the $\frac{k_{fluid}}{k_S}$ values of nanofluids of cylindrical nanoparticles. On the other hand, the empirical model described by Pakdaman et al.,[82] which is specific for multiwalled CNT (MWCNT), shows higher $\frac{k_{fluid}}{k_S}$ values than those of simulated nanofluids. The experimental values of a 3 wt % oil-based graphene nanofluid and 1 wt % oil-based copper nanofluid are higher than those of the simulated nanofluids, while 1 wt % PAO-2-based MWCNT nanofluid shows values closer to the simulations.[26,27,83] The discrepancies between the experimental ratio and the simulated ratio can be attributed to the large size distribution of nanoparticles (diameter ≥ 40 nm), the actual chemistry of the oil ($\rho \geq 0.85$ g cm^{-3} and $\eta \geq 130$ mPa s), and the stabilizing additives (e.g., lipophilic polymers) used to synthesize the experimental nanofluids.

The differences in the way solid nanoparticles conduct heat in oil could shed light on why the heat transfer properties are different for the different solid−liquid mixtures of nanofluids. In order to quantify the mechanism of heat transfer of the additives in the nanofluids, the phonon density of states (DOS) is computed. The vibrational DOS of a particular atom is computed using the Fourier transform of the velocity autocorrelation function as follows[87]

$$\mathrm{DOS} = \int \frac{\langle v(t_0)\cdot v(t_0 + t)\rangle}{\langle v(t_0)\cdot v(t_0)\rangle} e^{-2\pi i\omega t} \mathrm{d}t \tag{9}$$

Figure 10 shows the DOS of the different atoms in solvent S1 and the nanofluids CU1, GR1, and CN1. As observed in Figure 10, the frequencies of carbon are prominent in the lower frequencies between 0 and 40 THz, whereas those of hydrogen are present in the high-frequency region of 80−100 THz. In the case of CU1, the copper nanoparticles show DOS frequencies between 0 and 20 THz. In the cases of GR1 and CN1, the multiple peak frequencies generally coincide with the DOS of carbon atoms of the oil solvent. Here, it is to be mentioned that while copper demonstrates a single major peak, the carbon-based nanoparticles showcase multiple peaks at distinct frequencies. This could lead to the occupation of more phonon states in the case of 2D graphene and CNT, which in turn raises the specific heat capacity of the GR1 and CN1 nanofluids, as seen in Figure 9a.[88] However, a more accurate understanding of the phonon dispersion curves requires quantum mechanical studies that are out of the scope of the current investigation.

Meanwhile, the matching degree of DOS[89,90] is obtained using

$$\delta_{\mathrm{DOS}} = \frac{\int_0^\infty \mathrm{DOS}_{\mathrm{nano}}(f)\mathrm{DOS}_{\mathrm{C}}(f)\mathrm{DOS}_{\mathrm{H}}(f)\mathrm{d}f}{\int_0^\infty \mathrm{DOS}_{\mathrm{nano}}(f)\mathrm{d}f \int_0^\infty \mathrm{DOS}_{\mathrm{C}}(f)\mathrm{d}f \int_0^\infty \mathrm{DOS}_{\mathrm{H}}(f)\mathrm{d}f} \tag{10}$$

where $\mathrm{DOS}_{\mathrm{nano}}(f)$ represents the density of state of nanoparticle, $\mathrm{DOS}_{\mathrm{C}}(f)$ represents the DOS of carbon atoms, and $\mathrm{DOS}_{\mathrm{H}}(f)$ represents the DOS of hydrogen atoms of the solvent and the polymer molecules. Figure 11 depicts the δ_{DOS} values of the different nanofluids. It is evident that CU1 and CU2 exhibit the highest δ_{DOS} values at all the simulated temperatures, indicating that phonon transfer is easily facilitated between the nanoparticles and solvent atoms in reference to their heat transfer mechanism. Thus, the contribution of the DOS peak of nanoparticles at very low frequency to the overall thermal conductivity is greater. On the other hand, the δ_{DOS} values of GR1, CN1, GR2, and CN2 are lower than those of copper nanofluids, ranging between 0.97 at 313 K and 0.90 at 373 K. However, from Figure 9b, it is evident that higher values of thermal conductivity are observed for nanofluids consisting of 2D graphene and CNT. In other words, the high intrinsic k values of carbon allotropes compared to copper nanoparticles (ca. 4−5 times higher, as shown in Table S5 in Supporting Information) are able to compensate for higher interfacial Kapitza resistance.[29] Kapitza resistance is defined as the thermal resistance to the flow of heat at the interface between the solid nanoparticles and the surrounding media. Here, a significant difference in the mechanism of heat transfer between the metallic and carbon-based nanofluids is identified. It is to be pointed out that 2D graphene and CNT thermal properties are critically dependent on the size of the particles and surface modifications (such as dislocations, edge roughness, and vacancies) that may vary the DOS pattern.[88]

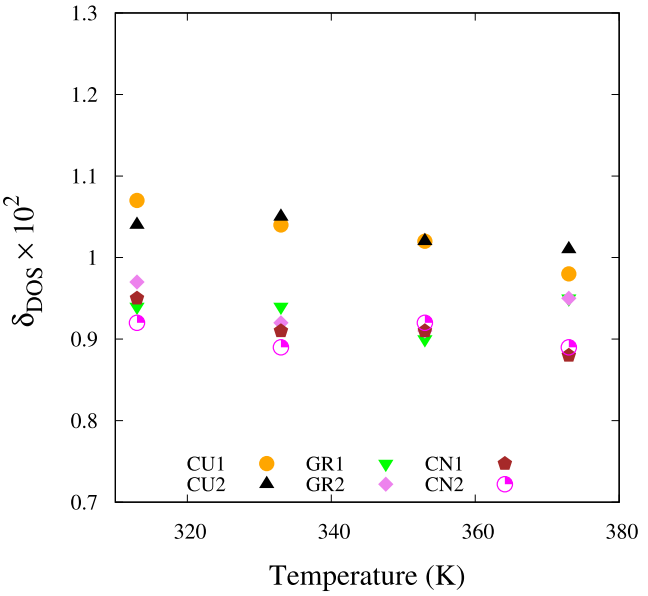

Figure 11. Matching degree of DOS, δ_{DOS}, of the simulated nanofluids as a function of temperature.

Heat Transfer Coefficient. In order to further understand the heat transfer enhancement potential of nanofluids while under convection conditions, the achieved heat transfer coefficient, h in each case, is computed by simulating Couette

https://doi.org/10.1021/acs.iecr.4c01832
Ind. Eng. Chem. Res. XXXX, XXX, XXX−XXX

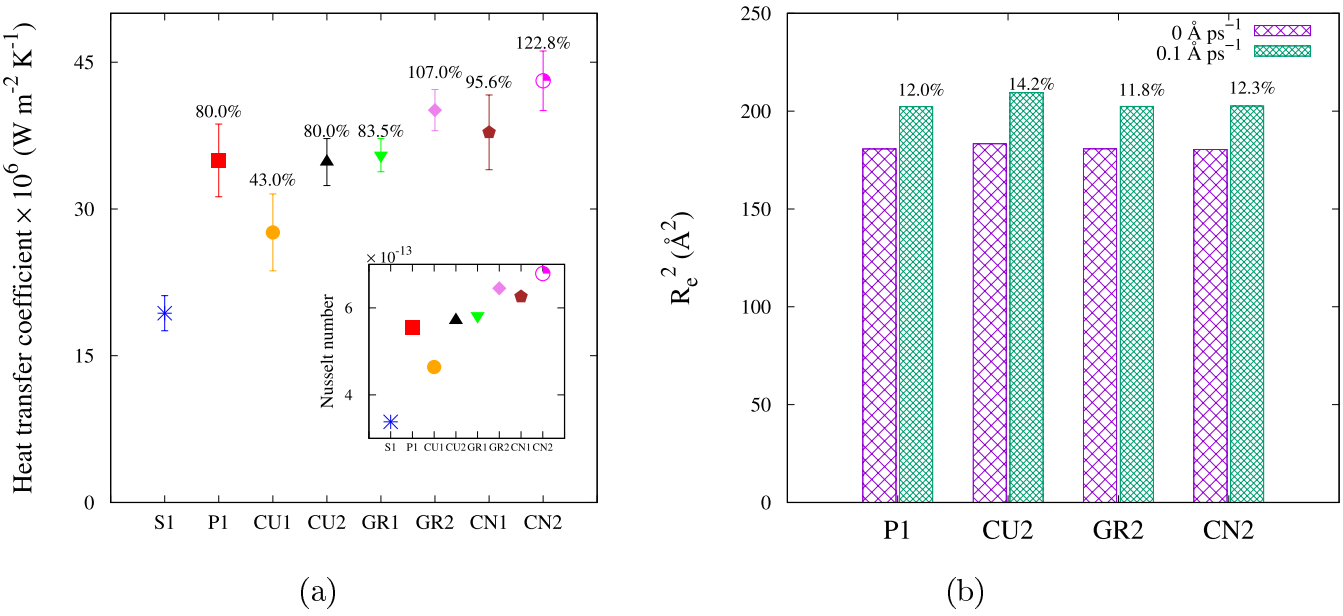

Figure 12. (a) Heat transfer coefficient (h) of the simulated fluids as a function of temperature. The error bars correspond to standard deviations from three independent runs. The inset shows the Nusselt number computed by using eq 11. The percentage value above each data point shows the enhancement of mean h values with respect to the corresponding value of S1. (b) Squared end-to-end distance R_e^2 for the different polymer-added fluids under the conditions of $v_{y,max}$ = 0 and 0.1 Å ps $^{-1}$.

flow between two Fe atomic layers. As described in the Simulation methodology section, the moving top Fe layer is heated to 373 K, and the stationary bottom Fe layer is maintained at 313 K. This leads to a temperature gradient, which, over a long time, becomes linear, as shown in Figure S4 in the Supporting Information. The shear rate applied in this exercise belongs to the shear thinning regime, as depicted in Figure S2. The corresponding velocity profile in the y-direction (v_y) is also shown in Figure S4. The heat flux vector in the liquid for such a system is computed as

$$\boldsymbol{J} = \frac{1}{A \cdot l}\left[\sum_i e_i \boldsymbol{v}_i + \frac{1}{2}\sum_{i<j} (\boldsymbol{F}_{ij} \cdot (\boldsymbol{v}_i + \boldsymbol{v}_j))\boldsymbol{r}_{ij}\right] \tag{11}$$

where e_i is per-atom total energy and the term $(\boldsymbol{F}_{ij} \cdot (\boldsymbol{v}_i + \boldsymbol{v}_j))\boldsymbol{r}_{ij}$ is the energy computed from the per-atom stress tensor.[91] A is the cross-sectional area of the simulation box normal to the heat flux direction with a length of fluid enclosure, l. Thus, the heat transfer coefficient in our case is computed as

$$h = \frac{q}{\Delta T} = -\frac{J_z}{\Delta t \Delta T} \tag{12}$$

with the time step of simulation—Δt and the temperature difference between the top and bottom layer of fluid being ΔT.[54] Furthermore, the apparent Nusselt number (Nu) is computed as

$$\mathrm{Nu} = \frac{hL}{k_{mean}} \tag{13}$$

where L is the characteristic length of the solid surface exposed to the fluid and k_{mean} is the mean of the thermal conductivity of the fluid at 313 and 373 K, as provided in Table S4. Based on the simulation box dimensions, as depicted in Figure 1, the value of L is equal to 32.5 Å.

The heat transfer coefficients of the different fluids simulated are shown in Figure 12a. The solvent S1 has an h value of 19.3 × 10^{-6} W m^{-2} K^{-1}. The addition of Cu nanoparticles increases the h value to 27.6 × 10^{-6} W m^{-2} K^{-1}, whereas GR1 shows a higher value of 35.5 × 10^{-6} W m^{-2} K^{-1}. However, the highest h value among the nanoparticles is observed when CNT is added to the oil, showing a consequent increase of 96%. Subsequently, the addition of an OCP polymer chain in the nanofluids shows a substantial increase in the heat transfer coefficients of the different nanofluids compared with the base solvent S1. While CU2 shows an increase of 80% of the h value compared to that of S1, GR2 shows an increase of 107%, and CN2 shows an increase of 122%. Thus, the addition of the OCP polymer chain improves the ability of the solutions to transfer heat, which, in turn, points to a thinner thermal boundary layer. The comparison of the Nusselt numbers, as shown in the inset of Figure 12a, demonstrates a similar trend as h values for the flows simulated here. To investigate the relation between the structure of the polymer and the enhancement of the h and Nu values in the dissolved nanofluids, computation of the end-to-end distance (R_e) of the OCP polymer chain is performed. Figure 12b shows the squared end-to-end distance and R_e^2 values under no flow condition in y-direction and under Couette flow at $v_{y,max}$ = 0.1 Å ps^{-1}. R_e^2 increases under the flow condition compared to the nonflow condition. This is a plausible reason contributing to the heat transfer coefficient enhancement in the polymer-additized nanofluids due to increasing polymer−solvent and polymer−nanoparticle interfacial heat transfer. An increase of 14.2% of the squared end-to-end distance of the polymer chain in CU2 showcases an additional 40% net enhancement in the h value compared to that of CU1. At the same time, an increase of 11.8 and 12.3% in the R_e^2 values demonstrate additional h value enhancements of 23.5 and 27.2% in GR2 and CN2, respectively. These variations indicate that the total enhancement of the heat transfer coefficients due to polymer addition is still limited by Kapitza resistance. It is to be noted here that the addition of viscoelastic polymer chains reduces turbulence intensity,[92] hindering heat transfer in turbulent flows. The

https://doi.org/10.1021/acs.iecr.4c01832
Ind. Eng. Chem. Res. XXXX, XXX, XXX−XXX

arguments outlined in this section are relevant to laminar flows, as simulated in this investigation.

Limitations. The presented research is concerned with nanofluids containing specific nanoparticles with sizes on the order of 1 nm. In real applications (or experiments), the nanoparticle size distributions range anywhere from 10 to 0.1 μm. The distinction is reflected in the order of magnitude differences in intrinsic thermal conductivities of the nanoparticles that are simulated (see Table S5) and which are available in the experimental literature.[50,51] The multibody force fields utilized for the solid particles are observed to underpredict the thermal conductivity and show dependence on the nanoparticle size.[93] The nanofluids may agglomerate or disintegrate during dynamic flow processes, which are not considered in the reported investigation. Such dynamic changes may affect the quantitative results of the reported heat transfer coefficient trends. Moreover, suspension-stabilizing agents or surfactants are an important component of practical nanofluids not considered here.[94] As reported by Sharma et al.,[95] the addition of these dispersants can lead to further modifications in the rheological behavior of the nanofluids, in essence affecting the heat transfer coefficients. However, the selection of an optimal surfactant chemistry can mitigate such effects.

CONCLUSIONS

Strong evidence for the suitability of oil-based dilute viscoelastic nanofluids for dielectric immersive-cooling applications is demonstrated by the present investigation. Among the nanoparticles dispersed, CNT and 2D Graphene showed higher values of thermal conductivity compared to metallic copper nanospheres within the temperature range of 313−373 K. Such a difference in impact is observed as a result of the different mechanisms of heat transfer between the nanoparticles and solvent PAO-2. While copper shows a higher DOS at lower frequencies, assisting in thermal conductivity enhancement, carbon-based nanoparticles are able to overcome the lower DOS matching degree with their high intrinsic thermal conductivity. Subsequently, the dilute nanofluids are shown to have higher heat transfer coefficients than PAO-2. Moreover, the addition of an OCP polymer chain is demonstrated to increase the heat transfer coefficients by more than 80% compared with the base solvent PAO-2 for the flows simulated here. The enhancement in the heat transfer coefficient is dependent on the extent of polymer chain expansion in combination with the interfacial Kapitza resistance of the nanoparticles and the surrounding media. For the practical use of such nanofluids for immersion-cooling applications, the selection of an appropriate suspension-stabilizing agent that does not negatively interfere with the heat transfer mechanisms requires further research.

ASSOCIATED CONTENT

Supporting Information

The Supporting Information is available free of charge at https://pubs.acs.org/doi/10.1021/acs.iecr.4c01832.

Force field details; comparison of thermal conductivities and viscosities; Carreau model parameters; and Couette flow temperature and velocity profiles (PDF)

AUTHOR INFORMATION

Corresponding Author

Ioannis K. Karathanassis − *School of Science and Technology, City, University of London, EC1 V 0HB London, U.K.*; Phone: +44 (0)20 7040 8172; Email: ioannis.karathanassis@city.ac.uk

Authors

Bharath Ravikumar − *School of Science and Technology, City, University of London, EC1 V 0HB London, U.K.*; orcid.org/0000-0001-7095-2195

Timothy Smith − *Lubrizol European Research and Development Centre, DE56 4AN Derbyshire, U.K.*

Manolis Gavaises − *School of Science and Technology, City, University of London, EC1 V 0HB London, U.K.*

Complete contact information is available at: https://pubs.acs.org/10.1021/acs.iecr.4c01832

Author Contributions

B.R.: Conceptualization, methodology, validation, data curation, formal analysis, investigation, writing, and visualization; I.K.: Conceptualization, resources, data curation, writing—review and editing supervision, project administration, and funding acquisition; T.S.: Methodology, investigation, resources, and writing—review and editing M.G.: Supervision, project administration, funding acquisition, and writing—review and editing supervision.

Notes

The authors declare the following competing financial interest(s): T. Smith is a full-time employee of Lubrizol Limited. All other authors declare no financial competing interests. All other authors declare no non-financial competing interests.

ACKNOWLEDGMENTS

The work has received funding from the EU Framework Programme for Research and Innovation HORIZON 2020 under the grant agreement no. 899659 (I-BAT project). The authors also acknowledge Hyperion HPC facility at City, University of London, and NHR-FAU HPC facility for their computational resources.

REFERENCES

(1) Tan, T.; Rennels, L.; Parthum, B. The social costs of hydrofluorocarbons and the benefits from their expedited phase-down. *Nat. Clim. Change* **2024**, *14*, 55−60.

(2) Woodcock, A. Hydrofluorocarbons, climate, and health—moving the Montreal Protocol beyond ozone-layer recovery. *N. Engl. J. Med.* **2023**, *388*, 2404−2406.

(3) Gota, S.; Huizenga, C.; Peet, K.; Medimorec, N.; Bakker, S. Decarbonising transport to achieve Paris Agreement targets. *Energy Effic.* **2019**, *12*, 363−386.

(4) Baysset, G.; Chessé, P.; Chalet, D.; Lefebvre, A. Optimal HEV cooling system design through a computer-aided virtual development chain. *Proc. Inst. Mech. Eng., Part D* **2023**, *237*, 655−667.

(5) Wang, Q.; Jiang, B.; Li, B.; Yan, Y. A critical review of thermal management models and solutions of lithium-ion batteries for the development of pure electric vehicles. *Renewable Sustainable Energy Rev.* **2016**, *64*, 106−128.

(6) Piao, C.; Chen, T.; Zhou, A.; Wang, P.; Chen, J. Research on electric vehicle cooling system based on active and passive liquid cooling. *J. Phys.: Conf. Ser.* **2020**, *1549*, No. 042146.

(7) Wang, T.; Tseng, K.; Zhao, J.; Wei, Z. Thermal investigation of lithium-ion battery module with different cell arrangement structures and forced air-cooling strategies. *Appl. Energy* **2014**, *134*, 229−238.
(8) Roe, C.; Feng, X.; White, G.; Li, R.; Wang, H.; Rui, X.; Li, C.; Zhang, F.; Null, V.; Parkes, M.; et al. Immersion cooling for lithium-ion batteries-A review. *J. Power Sources* **2022**, *525*, No. 231094.
(9) Wu, H.; Li, C.; Li, J. Heat transfer enhancement by pulsating flow of a viscoelastic fluid in a microchannel with a rib plate. *Nanoscale Microscale Thermophys. Eng.* **2022**, *26* (2-3), 112−128.
(10) Karathanassis, I.; Pashkovski, E.; Heidari-Koochi, M.; Jadidbonab, H.; Smith, T.; Gavaises, M.; Bruecker, C. Non-Newtonian flow of highly-viscous oils in hydraulic components. *J. Non-Newtonian Fluid Mech.* **2020**, *275*, No. 104221.
(11) Khan, M. B.; Sasmal, C.; Chhabra, R. Flow and heat transfer characteristics of a rotating cylinder in a FENE-P type viscoelastic fluid. *J. Non-Newtonian Fluid Mech.* **2020**, *282*, No. 104333.
(12) Cui, X.; Wang, J.; Xia, G. Enhanced thermal conductivity of nanofluids by introducing Janus particles. *Nanoscale* **2021**, *14*, 99−107.
(13) Choi, S. U. S.; Eastman, J. A. *Enhancing Thermal Conductivity of Fluids with Nanoparticles (No. ANL/MSD/CP-84938; CONF-951135-29)*; Argonne National Lab.(ANL): Argonne, IL (United States), 1995.
(14) Wen, D.; Ding, Y. Experimental investigation into convective heat transfer of nanofluids at the entrance region under laminar flow conditions. *Int. J. Heat Mass Transfer* **2004**, *47*, 5181−5188.
(15) Zeinali Heris, S.; Etemad, S. G.; Esfahany, M. N. Experimental investigation of oxide nanofluids laminar flow convective heat transfer. *Int. Commun. Heat Mass Transfer* **2006**, *33*, 529−535.
(16) Baby, T. T.; Ramaprabhu, S. Experimental investigation of the thermal transport properties of a carbon nanohybrid dispersed nanofluid. *Nanoscale* **2011**, *3*, 2208−2214.
(17) Branson, B. T.; Beauchamp, P. S.; Beam, J. C.; Lukehart, C. M.; Davidson, J. L. Nanodiamond nanofluids for enhanced thermal conductivity. *ACS Nano* **2013**, *7*, 3183−3189.
(18) Maheshwary, P.; Handa, C.; Nemade, K. A comprehensive study of effect of concentration, particle size and particle shape on thermal conductivity of titania/water based nanofluid. *Appl. Therm. Eng.* **2017**, *119*, 79−88.
(19) Apmann, K.; Fulmer, R.; Soto, A.; Vafaei, S. Thermal conductivity and viscosity: Review and optimization of effects of nanoparticles. *Materials* **2021**, *14*, 1291.
(20) Li, D.; Mahmoud, M. Z.; Suksatan, W.; Kuznetsova, M.; Abed, A. M.; Hekmatifar, M.; Toghraie, D.; Sabetvand, R. Thermal behavior of water base-fluid in the presence of graphene nanosheets and carbon nanotubes: A molecular dynamics simulation. *Case Stud. Therm. Eng.* **2021**, *28*, No. 101669.
(21) Izadkhah, M.-S.; Zeinali Heris, S. Influence of Al2O3 nanoparticles on the stability and viscosity of nanofluids: Insights from molecular dynamics simulation. *J. Therm. Anal. Calorim.* **2019**, *138*, 623−631.
(22) Shit, S. P.; Ghosh, N.; Pal, S.; Sau, K. Particle size and temperature effects on thermal conductivity of aqueous Ag nanofluids: modelling and simulations using classical molecular dynamics. *Eur. Phys. J. D* **2022**, *76*, 238.
(23) Yang, Y.; Zhang, Z. G.; Grulke, E. A.; Anderson, W. B.; Wu, G. Heat transfer properties of nanoparticle-in-fluid dispersions (nanofluids) in laminar flow. *Int. J. Heat Mass Transfer* **2005**, *48*, 1107−1116.
(24) Salman, B.; Mohammed, H.; Munisamy, K.; Kherbeet, A. S. Characteristics of heat transfer and fluid flow in microtube and microchannel using conventional fluids and nanofluids: a review. *Renewable Sustainable Energy Rev.* **2013**, *28*, 848−880.
(25) Senatore, A.; D'Agostino, V.; Petrone, V.; Ciambelli, P.; Sarno, M. Graphene oxide nanosheets as effective friction modifier for oil lubricant: materials, methods, and tribological results. *ISRN Tribol.* **2013**, *2013*, 425809.
(26) Cai, Z.; Tian, M.; Zhang, G. Experimental Study on the Flow and Heat Transfer of Graphene-Based Lubricants in a Horizontal Tube. *Processes* **2020**, *8*, 1675.
(27) Aberoumand, S.; Jafarimoghaddam, A. Experimental study on synthesis, stability, thermal conductivity and viscosity of Cu−engine oil nanofluid. *J. Taiwan Inst. Chem. Eng.* **2017**, *71*, 315−322.
(28) Jin, X.; Guan, H.; Wang, R.; Huang, L.; Shao, C. The most crucial factor on the thermal conductivity of metal-water nanofluids: Match degree of the phonon density of state. *Powder Technol.* **2022**, *412*, No. 117969.
(29) Alosious, S.; Kannam, S. K.; Sathian, S. P.; Todd, B. Nanoconfinement effects on the kapitza resistance at water-cnt interfaces. *Langmuir* **2021**, *37*, 2355−2361.
(30) Hong, T.-K.; Yang, H.-S.; Choi, C. Study of the enhanced thermal conductivity of Fe nanofluids. *J. Appl. Phys.* **2005**, *97*, No. 064311.
(31) Maxwell, J. C. *A Treatise on Electricity and Magnetism*; Clarendon Press, 1873; Vol. *1*.
(32) Hamilton, R. L.; Crosser, O. K. IEC fundamentals. *Int. Heat Mass Trans.* **1962**, *2*, 187−189.
(33) Davis, R. H. The effective thermal conductivity of a composite material with spherical inclusions. *Int. J. Thermophys.* **1986**, *7*, 609−620.
(34) Lu, S.-Y.; Lin, H.-C. Effective conductivity of composites containing aligned spheroidal inclusions of finite conductivity. *J. Appl. Phys.* **1996**, *79*, 6761−6769.
(35) Yu, W.; Choi, S. The role of interfacial layers in the enhanced thermal conductivity of nanofluids: a renovated Maxwell model. *J. Nanopart. Res.* **2003**, *5*, 167−171.
(36) Jang, S. P.; Choi, S. U. Role of Brownian motion in the enhanced thermal conductivity of nanofluids. *Appl. Phys. Lett.* **2004**, *84*, 4316−4318.
(37) Alghamdi, M.; Akbar, N. S.; Zamir, T.; Muhammad, T. Double layered combined convective heated flow of Eyring-Powell fluid across an elevated stretched cylinder using intelligent computing approach. *Case Stud. Therm. Eng.* **2024**, *54*, No. 104009.
(38) Akbar, N. S.; Zamir, T.; Akram, J.; Noor, T.; Muhammad, T. Simulation of hybrid boiling nano fluid flow with convective boundary conditions through a porous stretching sheet through Levenberg Marquardt artificial neural networks approach. *Int. J. Heat Mass Transfer* **2024**, *228*, No. 125615.
(39) Guo, J.; Zhao, Y.; Sun, B.; Wang, P.; Wang, Z.; Dong, H. Research progress of nano copper lubricant additives on engineering tribology. *Metals* **2021**, *11*, 2006.
(40) Kannan, G.; Karvembu, R.; Anand, R. Effect of metal based additive on performance emission and combustion characteristics of diesel engine fuelled with biodiesel. *Appl. Energy* **2011**, *88*, 3694−3703.
(41) Parvar, S.; da Silva, C. B.; Pinho, F. Thermal boundary layer of laminar flow of dilute polymer solution. *Int. J. Heat Mass Transfer* **2022**, *185*, No. 122248.
(42) Benda, R.; Bullen, J.; Plomer, A. Synthetics basics: Polyalphaolefins−base fluids for high-performance lubricants. *J. Synth. Lubr.* **1996**, *13*, 41−57.
(43) Ko, Y. S.; Kwon, W.-S.; No, M.-H.; Yim, J.-H. A Study on the control of microstructures of polyalphaolefins via cationic polymerization. *Polymer* **2015**, *39*, 346−352.
(44) Covitch, M. J. *Lubricant Additives*; Rudnick, L. R., Ed.; CRC Press, 2017; pp 225−246.
(45) Celata, G. P.; D'Annibale, F.; Mariani, A.; Sau, S.; Serra, E.; Bubbico, R.; Menale, C.; Poth, H. Experimental results of nanofluids flow effects on metal surfaces. *Chem. Eng. Res. Des.* **2014**, *92*, 1616−1628.
(46) Bree, G.; Horstman, D.; Low, C. T. J. Light-weighting of battery casing for lithium-ion device energy density improvement. *J. Energy Storage* **2023**, *68*, No. 107852.
(47) Mathas, D.; Holweger, W.; Wolf, M.; Bohnert, C.; Bakolas, V.; Procelewska, J.; Wang, L.; Bair, S.; Skylaris, C.-K. Evaluation of methods for viscosity simulations of lubricants at different temper-

https://doi.org/10.1021/acs.iecr.4c01832
Ind. Eng. Chem. Res. XXXX, XXX, XXX−XXX

atures and pressures: a case study on PAO-2. *Tribol. Trans.* **2021**, *64*, 1138−1148.
(48) Ravikumar, B.; Karathanassis, I. K.; Smith, T.; Gavaises, M. Dilute viscoelastic polymer solutions for dielectric heat transfer applications: A molecular dynamics study. *Int. J. Thermofluids* **2023**, *18*, No. 100333.
(49) Guo, Z.; Zhang, Y.; Wang, J.; Gao, C.; Zhang, S.; Zhang, P.; Zhang, Z. Interactions of Cu nanoparticles with conventional lubricant additives on tribological performance and some physicochemical properties of an ester base oil. *Tribol. Int.* **2020**, *141*, No. 105941.
(50) Elsaid, K.; Abdelkareem, M. A.; Maghrabie, H. M.; Sayed, E. T.; Wilberforce, T.; Baroutaji, A.; Olabi, A. Thermophysical properties of graphene-based nanofluids. *Int. J. Thermofluids* **2021**, *10*, No. 100073.
(51) Kwon, Y.-K.; Kim, P. Unusually High Thermal Conductivity in Carbon Nanotubes. In *High Thermal Conductivity Materials*; Springer: New York, NY, 2006; pp 227−265.
(52) Müller-Plathe, F. A simple nonequilibrium molecular dynamics method for calculating the thermal conductivity. *J. Chem. Phys.* **1997**, *106*, 6082−6085.
(53) Yeh, I.-C.; Berkowitz, M. L. Ewald summation for systems with slab geometry. *J. Chem. Phys.* **1999**, *111*, 3155−3162.
(54) Assadi, S.; Kalteh, M.; Bagheri Motlagh, M. Investigating convective heat transfer coefficient of nanofluid Couette flow in a nanochannel by molecular dynamics simulation. *Mol. Simul.* **2022**, *48*, 702−711.
(55) Sarkar, S.; Selvam, R. P. Molecular dynamics simulation of effective thermal conductivity and study of enhanced thermal transport mechanism in nanofluids. *J. Appl. Phys.* **2007**, *102* (7), 074302.
(56) Lindsay, L.; Broido, D. Optimized Tersoff and Brenner empirical potential parameters for lattice dynamics and phonon thermal transport in carbon nanotubes and graphene. *Phys. Rev. B* **2010**, *81*, No. 205441.
(57) Foiles, S. M.; Baskes, M.; Daw, M. S. Embedded-atom-method functions for the fcc metals Cu, Ag, Au, Ni, Pd, Pt, and their alloys. *Phys. Rev. B* **1986**, *33*, 7983.
(58) Heinz, H.; Vaia, R.; Farmer, B.; Naik, R. Accurate simulation of surfaces and interfaces of face-centered cubic metals using 12- 6 and 9- 6 Lennard-Jones potentials. *J. Phys. Chem. C* **2008**, *112*, 17281−17290.
(59) Luo, T.; Lloyd, J. R. Enhancement of thermal energy transport across graphene/graphite and polymer interfaces: a molecular dynamics study. *Adv. Funct. Mater.* **2012**, *22*, 2495−2502.
(60) Erhart, P.; Albe, K. Analytical potential for atomistic simulations of silicon, carbon, and silicon carbide. *Phys. Rev. B* **2005**, *71*, No. 035211.
(61) Tersoff, J. Empirical interatomic potential for carbon, with applications to amorphous carbon. *Phys. Rev. Lett.* **1988**, *61*, 2879.
(62) Brenner, D. W. Empirical potential for hydrocarbons for use in simulating the chemical vapor deposition of diamond films. *Phys. Rev. B* **1990**, *42*, 9458.
(63) Shen, X.-Y.; Hekmatifar, M.; Shukor, M. Y. A.; Alizadeh, Aa.; Sun, Y.-L.; Toghraie, D.; Sabetvand, R. Molecular dynamics simulation of water-based Ferro-nanofluid flow in the microchannel and nanochannel: Effects of number of layers and material of walls. *J. Mol. Liq.* **2021**, *338*, No. 116924.
(64) Anitha, K.; Namsani, S.; Singh, J. K. Removal of heavy metal ions using a functionalized single-walled carbon nanotube: a molecular dynamics study. *J. Phys. Chem. A* **2015**, *119*, 8349−8358.
(65) Wang, L.; Jin, J.; Yang, P.; Zong, Y.; Peng, Q. Graphene adhesion mechanics on iron substrates: insight from molecular dynamic simulations. *Crystals* **2019**, *9*, 579.
(66) He, X.; Bai, Q.; Shen, R. Atomistic perspective of how graphene protects metal substrate from surface damage in rough contacts. *Carbon* **2018**, *130*, 672−679.
(67) Tersoff, J. Modeling solid-state chemistry: Interatomic potentials for multicomponent systems. *Phys. Rev. B* **1989**, *39*, 5566.
(68) Jorgensen, W. L.; Maxwell, D. S.; Tirado-Rives, J. Development and testing of the OPLS all-atom force field on conformational energetics and properties of organic liquids. *J. Am. Chem. Soc.* **1996**, *118*, 11225−11236.
(69) Siu, S. W. I.; Pluhackova, K.; Böckmann, R. A. Optimization of the OPLS-AA force field for long hydrocarbons. *J. Chem. Theory Comput.* **2012**, *8*, 1459−1470.
(70) Wu, L.; Song, B.; Keer, L. M.; Gu, L. Molecular dynamics investigation of graphene nanoplate diffusion behavior in poly-α-olefin lubricating oil. *Crystals* **2018**, *8*, 361.
(71) Dou, X.; Koltonow, A. R.; He, X.; Jang, H. D.; Wang, Q.; Chung, Y.-W.; Huang, J. Self-dispersed crumpled graphene balls in oil for friction and wear reduction. *Proc. Natl. Acad. Sci. U. S. A.* **2016**, *113*, 1528−1533.
(72) Zhang, L.; Jing, Y.; Qu, P.; Wang, W.; Yao, X.; Tian, L. Effect of microstructure of nanoparticles and surrounding alcohol groups on energy transfer efficiency. *Appl. Therm. Eng.* **2022**, *215*, No. 119031.
(73) Kuziel, A. W.; Milowska, K. Z.; Chau, P.-L.; Boncel, S.; Koziol, K. K.; Yahya, N.; Payne, M. C. The true amphipathic nature of graphene flakes: a versatile 2D stabilizer. *Adv. Mater.* **2020**, *32*, No. 2000608.
(74) Rivet, J.-P.Green−Kubo Formalism for Lattice Gas Hydrodynamics and Monte-Carlo Evaluation of Shear Viscosities. In *Lattice Gas Methods For Partial Differential Equations*; CRC Press, 2019; Vol. *1*, pp 401−414.
(75) Santak, P.; Conduit, G. Enhancing NEMD with automatic shear rate sampling to model viscosity and correction of systematic errors in modeling density: Application to linear and light branched alkanes. *J. Chem. Phys.* **2020**, *153*, No. 014102.
(76) Allen, M. P.; Tildesley, D. J. *Computer Simulation of Liquids*; Oxford University Press, 2017.
(77) Mohebbi, A. Prediction of specific heat and thermal conductivity of nanofluids by a combined equilibrium and non-equilibrium molecular dynamics simulation. *J. Mol. Liq.* **2012**, *175*, 51−58.
(78) Caleman, C.; Van Maaren, P. J.; Hong, M.; Hub, J. S.; Costa, L. T.; Van Der Spoel, D. Force field benchmark of organic liquids: density, enthalpy of vaporization, heat capacities, surface tension, isothermal compressibility, volumetric expansion coefficient, and dielectric constant. *J. Chem. Theory Comput.* **2012**, *8*, 61−74.
(79) Baird, D.; Ferentinos, J. Application of MIL-C-87252 in F-22 liquid cooling system. *SAE Trans.* **1998**, *107*, 247−259.
(80) Singh, T.; Almanassra, I. W.; Al-Ansari, T.; McKay, G.; Atieh, M. A. Performance investigation of graphene oxide-based water/oil nanofluids for high pressure and high temperature solar thermal technologies for sustainable energy systems. *FlatChem* **2022**, *35*, No. 100420.
(81) Hone, J. *Carbon Nanotubes: Synthesis, Structure, Properties, and Applications*; Dresselhaus, M. S.; Dresselhaus, G.; Avouris, P., Eds.; Springer Berlin Heidelberg: Berlin, Heidelberg, 2001; pp 273−286.
(82) Fakoor Pakdaman, M.; Akhavan-Behabadi, M.; Razi, P. An experimental investigation on thermo-physical properties and overall performance of MWCNT/heat transfer oil nanofluid flow inside vertical helically coiled tubes. *Exp. Therm. Fluid Sci.* **2012**, *40*, 103−111.
(83) Narvaez, J. A. Thermal conductivity of poly-alpha-olefin (pao)-based nanofluids, M.Sc. thesis; University of Dayton2010.
(84) Pekar, L. *Advanced Analytic and Control Techniques for Thermal Systems with Heat Exchangers*; Academic Press, 2020.
(85) Komatsu, T. S.; Nakagawa, N.; Sasa, S.-i.; Tasaki, H. Steady-state thermodynamics for heat conduction: microscopic derivation. *Phys. Rev. Lett.* **2008**, *100*, No. 230602.
(86) Cui, W.; Bai, M.; Lv, J.; Li, G.; Li, X. On the influencing factors and strengthening mechanism for thermal conductivity of nanofluids by molecular dynamics simulation. *Ind. Eng. Chem. Res.* **2011**, *50*, 13568−13575.
(87) Dickey, J. M.; Paskin, A. Computer simulation of the lattice dynamics of solids. *Phys. Rev.* **1969**, *188*, 1407.

https://doi.org/10.1021/acs.iecr.4c01832
Ind. Eng. Chem. Res. XXXX, XXX, XXX−XXX

(88) Pop, E.; Varshney, V.; Roy, A. K. Thermal properties of graphene: Fundamentals and applications. *MRS Bull.* **2012**, *37*, 1273−1281.
(89) Lan, J.; Li, B. Thermal rectifying effect in two-dimensional anharmonic lattices. *Phys. Rev. B* **2006**, *74*, No. 214305.
(90) Chen, J.; Zhang, G.; Li, B. Tunable thermal conductivity of Si1-xGex nanowires. *Appl. Phys. Lett.* **2009**, *95*, No. 073117.
(91) Rapaport, D. C. *The Art of Molecular Dynamics Simulation*; Cambridge University Press, 2004.
(92) Ptasinski, P. K.; Boersma, B.; Nieuwstadt, F.; Hulsen, M.; Van den Brule, B.; Hunt, J. Turbulent channel flow near maximum drag reduction: simulations, experiments and mechanisms. *J. Fluid Mech.* **2003**, *490*, 251−291.
(93) Rezaee, F.; Yousefi, F.; Khoeini, F. Heat transfer in strained twin graphene: A non-equilibrium molecular dynamics simulation. *Phys. A* **2021**, *564*, No. 125542.
(94) Shibata, K.; Shimoyama, Y.; Orita, Y. Prediction of Nanoparticle Dispersion by Machine Learning Using Various Molecular Descriptors. *Ind. Eng. Chem. Res.* **2023**, *62*, 19683−19689.
(95) Sharma, A. K.; Tiwari, A. K.; Dixit, A. R. Rheological behaviour of nanofluids: A review. *Renewable Sustainable Energy Rev.* **2016**, *53*, 779−791.

https://doi.org/10.1021/acs.iecr.4c01832
Ind. Eng. Chem. Res. XXXX, XXX, XXX−XXX